JOURNAL OF THERMOPHYSICS AND HEAT TRANSFER
Vol. 21, No. 4, October–December 2007

Flow and Heat Transfer Prediction in Rotating Rectangular Pin-Fin Channels (AR = 10:1)

Mohammad S. Al-Qahtani* and Mehaboob Basha†
King Fahd University of Petroleum and Minerals, Dhahran 31261, Saudi Arabia

DOI: 10.2514/1.25580

Computations were performed to study the three-dimensional turbulent flow and heat transfer in a rotating narrow rectangular channel with staggered arrays of pin fins. The channel aspect ratio is 10:1, the pin length to diameter ratio is 1.0, and the pin spacing to hydraulic diameter ratio is 3.0 in both the streamwise (S_L/D_h) and spanwise (S_T/D_h) directions. Various combinations of rotation numbers and coolant-to-wall density ratios were examined. A total of seven calculations have been performed with various rotation numbers and inlet coolant-to-wall density ratios. The rotation number and density ratio varied from 0.0 to 0.14 and from 0.1 to 0.40, respectively. The Reynolds number is fixed to 10,000. A finite volume code, FLUENT is used to predict the flow and heat transfer. The Reynolds stress model in conjunction with a two-layer model is used to compute the turbulent flow and heat transfer in the rotating channel. The computational results are in good agreement with experimental data.

Nomenclature

AR	=	channel aspect ratio
Cp	=	specific heat, J/kg · K
D, d	=	pin diameter, m
D_h	=	hydraulic diameter, m
H	=	pin length, m
h	=	heat transfer coefficient, W/m^2 · K
k	=	thermal conductivity, W/m · K
L	=	length of the duct, m
Nu	=	Nusselt number in fully developed turbulent nonrotating tube flow, hD_h/k
Nu_0	=	Nusselt number, hD_h/k
R_r	=	radius from axis of rotation, m
Re	=	Reynolds number, $\rho W_b D_h/\mu$
Ro	=	rotation number, $\Omega D_h/W_b$
S	=	arc length, m
S_L	=	pin longitudinal pitch, m
S_T	=	pin transverse pitch, m
T	=	local coolant temperature, K
T_i	=	inlet coolant temperature, K
T_w	=	wall temperature, K
u, v, and w	=	the mean velocities in x, y, and z directions, respectively, m/s
u_m	=	maximum velocity between pin fins, m/s
W_b	=	bulk velocity, m/s
β	=	angle of channel orientation measured from direction of rotation, deg
$\Delta\rho/\rho$	=	inlet coolant-to-wall density ratio, $(T_w - T_i)/T_w$
θ	=	dimensionless temperature, $[(T - T_i)/(T_W - T_i)]$
ρ	=	density of fluid, kg/m^3
υ	=	dynamic viscosity of the coolant, m^2/s
Ω	=	rotational speed, rad/s

Received 2 June 2006; revision received 8 February 2007; accepted for publication 16 March 2007.

*Assistant Professor, Department of Mechanical Engineering; mqahtani@kfupm.edu.sa.

†Research Engineer, Research Institute, Mechanical Engineering Department.

Introduction

Gas turbine stages are being designed to operate at increasingly higher inlet temperatures to improve thermal efficiencies. Sophisticated cooling techniques must be employed to cool the components to maintain the performance requirements. One method for cooling the turbine blades is internal cooling. With internal blade cooling, a small amount of air is extracted from the compressor, and the air is injected into the blades. Through forced convection, the coolant air removes heat from the walls of the blade. The narrow trailing edge of the turbine blade poses many challenges from both a cooling and a manufacturing view. The trailing edge is very narrow, so the typical cooling techniques of jet impingement and ribbed channels cannot be employed due to manufacturing constraints. Pin fins provide solutions to these problems. The use of pin fins to enhance heat transfer in cooling channels has been the focus of many studies throughout the years.

Many experimental investigations have proven that pin fins perform better in low aspect ratio (AR) channels for gas turbine blades. Metzger et al. [1] studied the developing heat transfer of short pin fins in stationary staggered arrays. They observed that the heat transfer coefficient gradually increases over the first several rows of pins, reaches a maximum around the third row, and gradually decreases through the remaining rows of the array. Metzger and Haley [2] then studied the effects of pin material and pin spacing on heat transfer in staggered arrays. They found that the Nusselt number values for the nonconducting pin fins closely followed the values of the conducting pin fins. They also showed that as the streamwise spacing was increased, the Nusselt number values decreased. Later, Metzger et al. [3] examined the row resolved heat transfer variation in pin-fin arrays. VanFossen [4] also investigated stationary cooling channels with pin-fin arrays. The study showed that the heat transfer from an array of short pins is lower than the heat transfer from an array of long pins. It was also found that the heat transfer coefficients on the pin surface were approximately 35% greater than those on the endwall. In a later study, Brigham and VanFossen [5] investigated the effect of pin-fin length on the heat transfer coefficient and concluded that the pin height-to-diameter ratio is the dominant factor affecting the amount of heat transferred from short pin-fin arrays (endwalls included). With the mass transfer technique, Chyu and Goldstein [6] observed the peak distribution of the Sherwood number and concluded that the staggered pin arrangement performs better than the inline arrangement. In more recent studies, Chyu et al. [7] investigated the effect of pin shape on heat transfer. They concluded that the cubic pin fin yields the highest heat transfer (in both staggered and inline arrays), followed by the diamond and then the circular pin fins. Chyu et al. [8] also studied the heat transfer

contribution of pin fins and endwalls in pin-fin arrays. This study found that conducting pin fins have a significantly higher heat transfer coefficient (10 to 20%) than the endwalls. Uzol and Camci [9] investigated the endwall heat transfer and total pressure loss within various arrays of pin fins. By comparing the heat transfer enhancement of circular pins and two elliptical pin-fin arrays, they found that the heat transfer in the wake of circular pins is 25% higher than that of the elliptical arrays. However, the elliptical geometry is viewed as a more desirable configuration due to the relative small pressure drop penalty (when compared to the circular array). Hwang and Lui [10] and Hwang et al. [11] presented experimental heat transfer and pressure drop results for airflows through trapezoidal pin-fin channels with the liquid crystal technique. They concluded that a straight wedge duct with a staggered pin array produces the highest heat transfer coefficient enhancement with a moderate pressure drop penalty. In an experiment conducted by Willett and Bergles [12], the heat transfer in rotating channels with conducting pin fins was studied. They found that the heat transfer enhancement due to rotation and buoyancy was much less than the enhancement observed from their study of a smooth narrow duct [13]. They showed that pin fins significantly reduce the effect of rotation, but they do not eliminate the effect. Wright et al. [14] studied a staggered array of pins under the rotating condition and found that 1) rotation enhances the heat transferred from the pin-fin channels 1.5 times that of the stationary pin-fin channels. 2) Overall, rotation enhances the heat transfer from all surfaces in both the smooth and pin-fin channels. 3) As the rotation number increases, spanwise variation increases in all channels.

Although heat transfer and pressure drop results are available in the open literature for flows through pin-fin channels, there are few

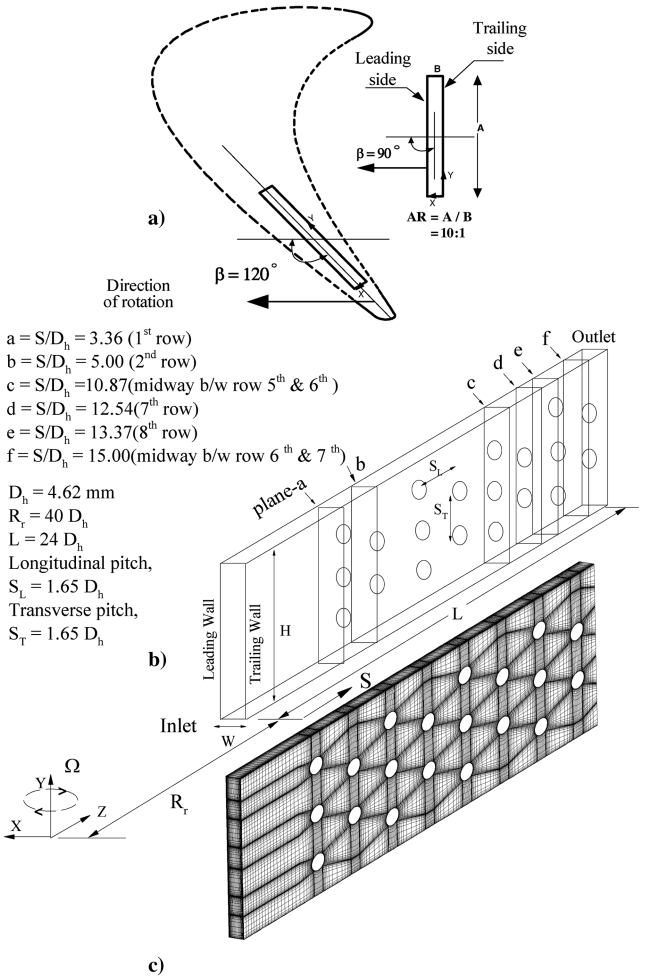

Fig. 1 Pin-fin channel aspect ratio (AR) 10:1: a) computational grid; b) geometry; c) location of the tilted cooling channel in a turbine blade.

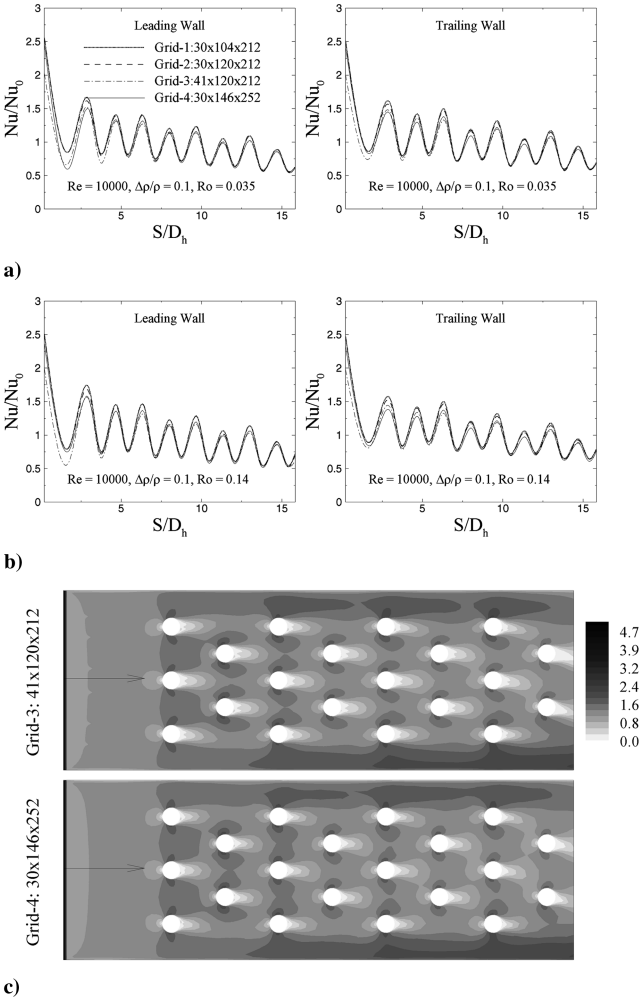

Fig. 2 Grid independence test. $Re = 10,000$ and $\Delta\rho/\rho = 0.1$: a) leading wall; b) trailing wall; c) normalized velocity contours on a plane midway between the leading and the trailing walls.

data available on the effects of rotation on the heat transfer and flow distributions for pin-fin channels. Furthermore, most of the experimental investigations for rotating pin-fin channels are limited to relatively low rotation number and low Reynolds number

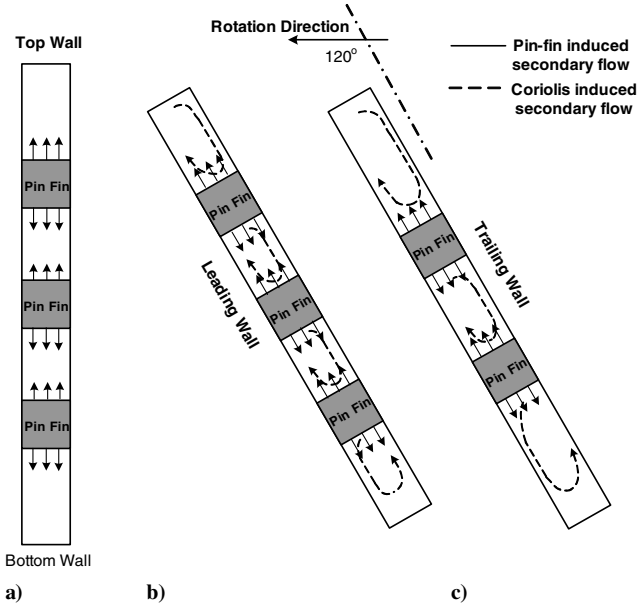

Fig. 3 Conceptual view of secondary flow induced by pin fins and Coriolis force.

conditions and provide only regionally averaged Nusselt number distributions. Therefore, it is desirable to use advanced numerical methods to facilitate more detailed understanding of the three-dimensional flow and heat transfer characteristics for pin-fin channels under high rotation number, high density ratio, and high Reynolds number conditions.

During the past decade, numerical methods have been used extensively for the prediction of three-dimensional flow and heat transfer in rotating rectangular channels with rib turbulators under various combinations of rotation number, Reynolds number, channel aspect ratio, and channel orientation. However, there are very few numerical studies on the pin-fin channels. Moreover, the few numerical studies in the literature primarily focus on the cooling techniques in electric circuit cooling or the shell and tube heat exchangers. Although there are some similarities with the pin-fin channels in gas turbine blades, these simulation results are not directly applicable for turbine blade cooling applications at high Reynolds number and high rotation number conditions. Donahoo et al. [15] employed a Galerkin finite element procedure to perform a 2-D study of a staggered cross pin array to determine an optimal row spacing considering both heat dissipation and required pumping power. Subsequently, Donahoo et al. [16] performed a 3-D calculation with the k–ε turbulence model to study the same problem including the endwall effects. More recently, Hamilton et al. [17] used the ANSYSTM commercial code to model the incompressible fluid flow in a pin-fin channel using the standard k–ε turbulence model in conjunction with the Van Driest coupling model for the wall region. Benhamadouche and Laurence [18] applied large eddy simulation (LES), coarse LES, and Reynolds stress turbulence model (RSTM) to compute flow across a tube bundle. Their main focus was to compare the capability of LES and RSTM results. It was shown that the LES results on the fine mesh are comparable to direct numerical simulation (DNS) and experiments and reasonable agreement is still achieved with a coarse mesh. The RSTM also produced satisfactory results in 3-D but showed no advantage over the LES when the grid was coarsened. Hassan and Barsamian [19] used LES to simulate the flow in a three-dimensional tube bundle. The calculations are consistent with the experimental data. The flapping effect in the tube wake is reported in the research. Recently, Su et al. [20] numerically studied flow and heat transfer in a rotating rectangular channel with staggered arrays of pin fins. They found that 1) the Nusselt number ratio reaches a maximum value around the third row and decreases slightly toward the channel exit. 2) Both the rotation and density ratio have only minor effects on the heat transfer enhancement. 3) High Reynolds numbers tend to reduce the heat transfer enhancement effect of the pin fins.

It is intended in this paper to study numerically the pin-fin channel configuration of Willett and Bergles [12]. The primary objective of the present study is to predict the three-dimensional flow and heat

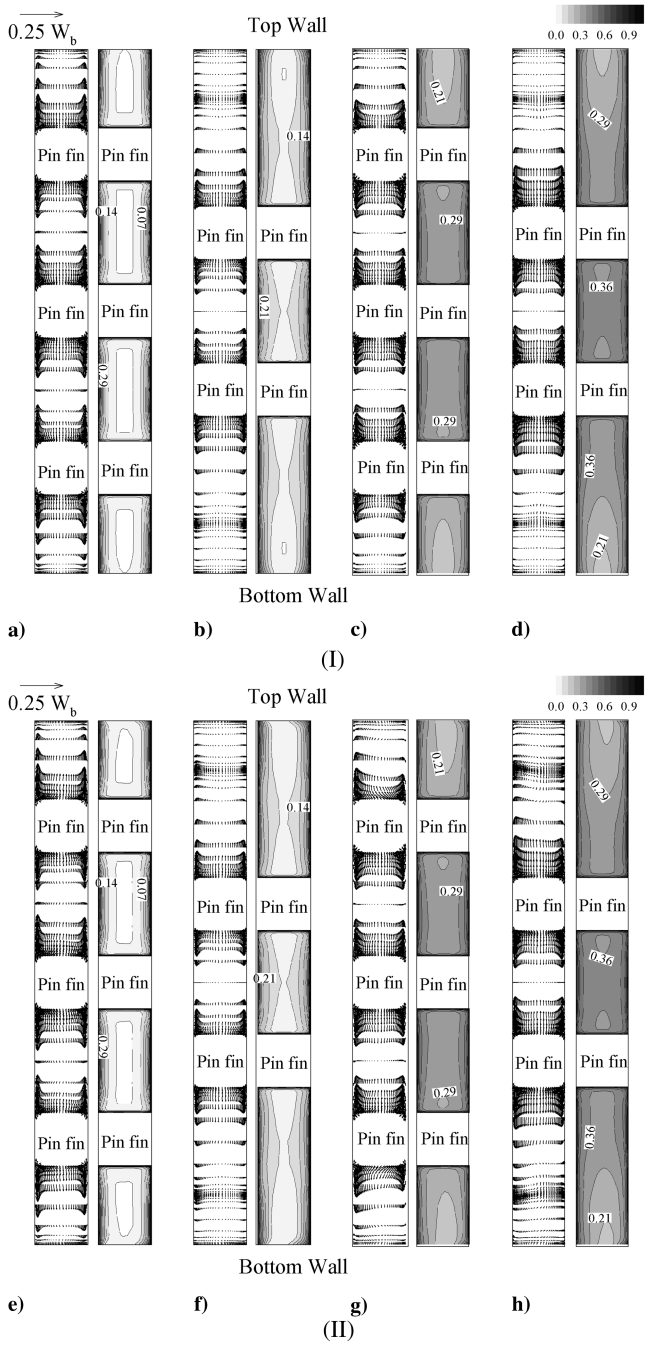

Fig. 4 Secondary velocity vectors and dimensionless temperature $[\theta = (T - Ti)/(Tw - Ti)]$ contours. $Re = 10,000$: (I) $Ro = 0.0$ and $\Delta\rho/\rho = 0.1$; (II) $Ro = 0.035$, $\beta = 90$ deg, and $\Delta\rho/\rho = 0.1$.

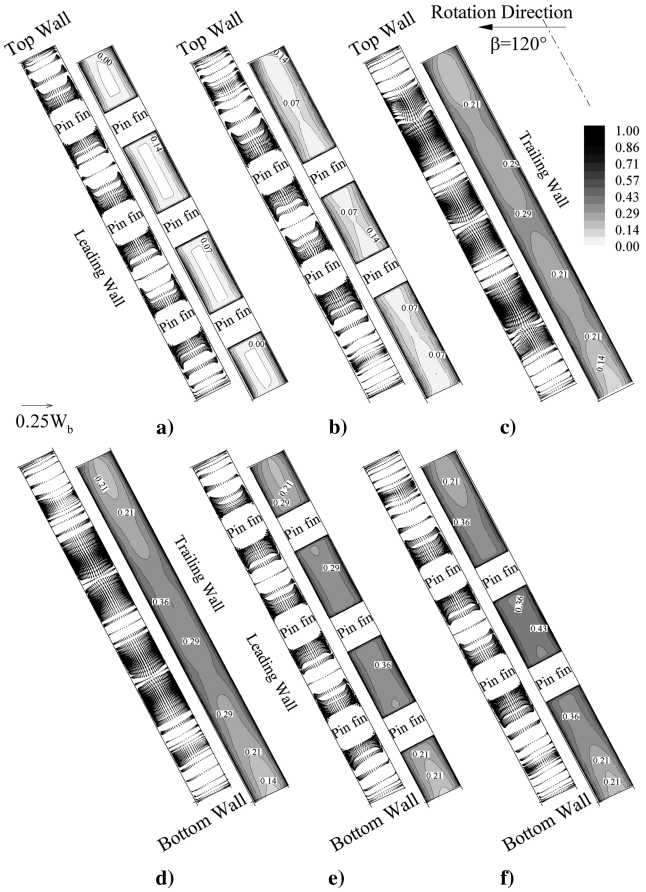

Fig. 5 Secondary velocity vectors and dimensionless temperature $[\theta = (T - T_i)/(T_w - T_i)]$ contours. $Re = 10,000$, $Ro = 0.035$, $\beta = 120$ deg, and $\Delta\rho/\rho = 0.1$.

transfer for the rotating/nonrotating pin-finned one-pass rectangular channel (AR = 10:1) with the two channel orientation ($\beta = 90$ and 120 deg) and compare with available experiment data.

Numerical Solution

Problem Description

Figure 1a shows the location of the tilted cooling channel in a turbine blade, whereas Fig. 1b shows the channel geometry. The cooling passage configuration is a pin-fin rectangular passage with AR of 10:1, oriented such that the long sides of the duct cross section are at $\beta = 90$ deg (in one case) and $\beta = 120$ deg to the direction of the blade tangential direction. The first configuration (i.e., $\beta = 90$ deg) is unlikely to be found in a cooled gas turbine blade, except in an unconventional design. However, it is used here for comparison with the other configuration ($\beta = 120$ deg). The $\beta = 120$ deg configuration is found at the trailing edge region of a blade. Two of the four sidewalls, in the rotational direction, are denoted as the leading and the trailing walls, respectively, while the other two sidewalls are denoted as the top and the bottom walls. The channel hydraulic diameter D_h is 4.62 mm. The distance from the inlet of the channel to the axis of rotation (Y axis) is given by $R_r/D_h = 41.20$ and the length of the channel is given as $L/D_h = 24.74$. The test channel of Willett and Bergles [12] contains 13 rows of pin fins, which are arranged in a staggered manner on the heated walls. Because of limitations in the computation resources, a domain with the first eight rows of the pin-fin channel is considered. The reason for considering only eight rows is a compromise between the limited computation resources and knowing that the flow becomes fully developed after the fourth row as found by Willett and Bergles [12]. The array of the pin-fin elements is composed of eight rows with three pin fins per row (three/two because of the staggered array). The pin-fin geometry is determined by the pin-fin diameter ($D = 0.55D_h$) and the pin-fin height ($H = D$), pin longitudinal pitch ($S_L = 1.65D_h$) and the pin transverse pitch ($S_T = 0.82D_h$). The cross-sectional planes at which results are presented are at axial locations $S/D_h = 3.36$ (first row), 5.00 (second row), 10.87 (midway between the fifth and sixth rows), 13.37 (at the eighth row), 12.54 (seventh row), and 15.00 (midway between the sixth and seventh rows), respectively.

Physical Properties

To validate our results, the geometry and physical properties are chosen similar to those used in the experiment of Willett and Bergles [12]. The physical properties of R134a are used, and the density variation with temperature is obtained using ideal gas law, that is, $\rho = P/RT$, where T, P, and R are local temperature, local pressure, and gas constant, respectively. ($\mu = 1.1879 \times 10^{-5}$ kg/m s, $k = 0.013538$ W/m · K, and $Cp = 854$ J/kg · K).

Computational Grid Detail

A finite volume code, FLUENT is used to predict flow and heat transfer characteristics. The grid was generated iteratively using gambit software. Figure 1c shows a nonuniform computational grid of the eight row pin-fin rectangular channel. The computation grid has 20 pin fins of diameter $D = 2.54$ mm, which are arranged in a staggered way on the heated walls. The Reynolds stress model in conjunction with a two-layer approach is used. The minimum grid spacing (first node from the wall) in the near-wall region is maintained at a reasonable distance, which corresponds to a wall coordinate y^+ of the order of 1. The mesh is structured with grid skewness that does not exceed 0.5 in the whole domain. The number of grid points in the streamwise direction is 212 and in the cross stream plane is 41 × 120. In all calculations, a convergence criterion for both the mean flow and turbulent quantities was set at 10^{-5}. The

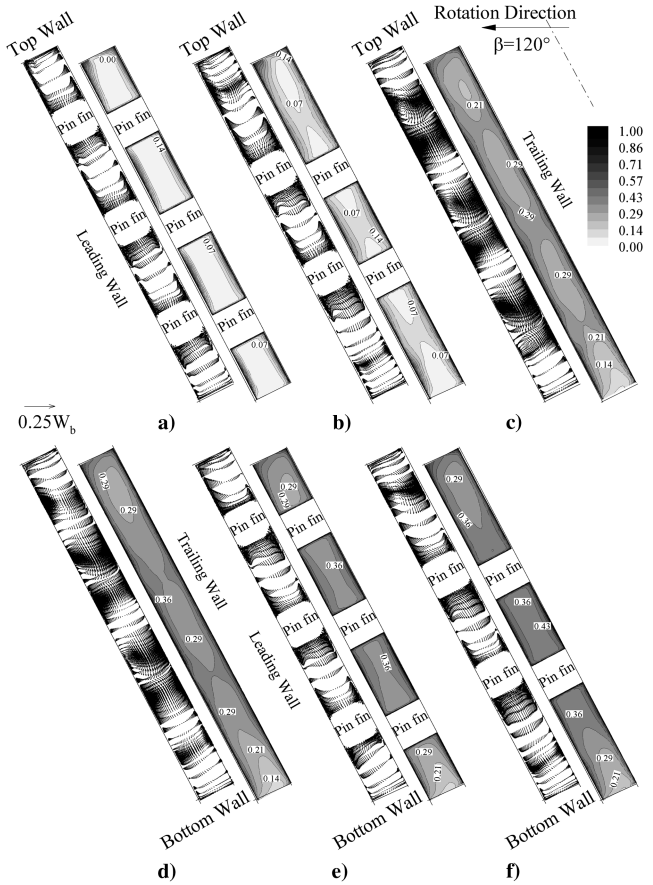

Fig. 6 Secondary velocity vectors and dimensionless temperature $[\theta = (T - T_i)/(T_w - T_i)]$ contours. $Re = 10,000$, $Ro = 0.14$, $\beta = 120$ deg, and $\Delta\rho/\rho = 0.1$.

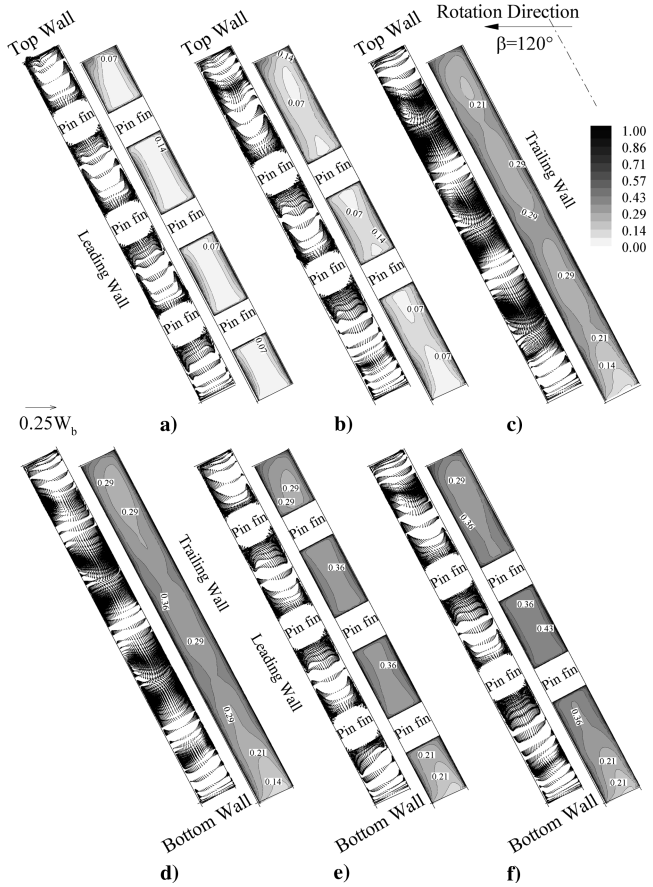

Fig. 7 Secondary velocity vectors and dimensionless temperature $[\theta = (T - T_i)/(T_w - T_i)]$ contours. $Re = 10,000$, $Ro = 0.14$, $\beta = 120$ deg, and $\Delta\rho/\rho = 0.4$.

Table 1 Summary of cases, $Re = 10,000$

Case	Rotation no., Ro	Density ratio, $\Delta\rho/\rho$	β
1	0.000	0.1	——
2	0.035	0.1	90 deg
3	0.035	0.1	120 deg
4	0.070	0.1	120 deg
5	0.140	0.1	120 deg
6	0.140	0.2	120 deg
7	0.140	0.4	120 deg

computational domain with eight rows of staggered pin fins is considered and meshed (structured) which resulted in 1,043,040 cells.

Grid Independence Test

A grid independency test was carried out on the pin-fin channel at two rotation numbers, $Ro = 0.035$ and 0.14 keeping the density ratio and the orientation angle constant, namely, $\Delta\rho/\rho = 0.1$ and $\beta =$ 120 deg, respectively. The tested grid sizes are $30 \times 104 \times 212$, $30 \times 120 \times 212$, $41 \times 120 \times 212$, and $30 \times 146 \times 252$. From now on, these grids will be referred to as grid-1, grid-2, grid-3, and grid-4, respectively. The parameters used to check the grid independency are the Nusselt number and the mean velocity. It can be seen from Figs. 2a and 2b that the spanwise Nusselt number profiles obtained from grid-3 and grid-4 are overlapping at both low and high rotation numbers. To check the grid independency in the y and z directions, a comparison is made between grid-2 and grid-4. The percentage difference of the averaged Nusselt number on the leading and trailing walls is less than 2%. To check the grid independency in the x direction, a comparison is made between grid-3 and grid-4. It can be noticed that the Nusselt number of the leading and trailing walls which is obtained from grid-3 (which has 41 nodes in the x direction) is 6% lower than the Nusselt number obtained from grid-4 (which has 30 nodes in the x direction). This indicates that grid-3 (which was used in the present study) is also grid independent in the x direction. Figure 2c shows a comparison of normalized velocity contours on a plane midway between the leading and the trailing walls, obtained from grid-3 and grid-4. The corresponding CPU time on xeon 3.06 GHz/2 GB RAM computers is about 26 h for convergence.

Boundary Condition

At the inlet ($z = 0$), a uniform velocity profile is used for the w component while the u, v components are assumed to be zero. The turbulent intensity of 4% is assumed at the inlet, which is specified using turbulent intensity and a hydraulic diameter option available in FLUENT. The FLUENT code does not allow the use of a zero outlet boundary condition if ideal gas law was used to compute the density. Because of this, pressure is fixed to atmospheric pressure. The Reynolds number based on a channel hydraulic diameter is fixed at 10,000. At walls, the no-slip condition is used in conjunction with the two-layer approach. The coolant fluid at the inlet of the channel is at a uniform temperature $T = T_i$, the top and the bottom walls were thermally insulated with a zero heat flux boundary condition, while the leading wall, trailing wall, and pin-fin surfaces are kept at constant temperature T_w.

Method of Solution

The governing (Reynolds-averaged Navier–Stokes) equations for mean flow variables are mentioned in [21]. These equations in

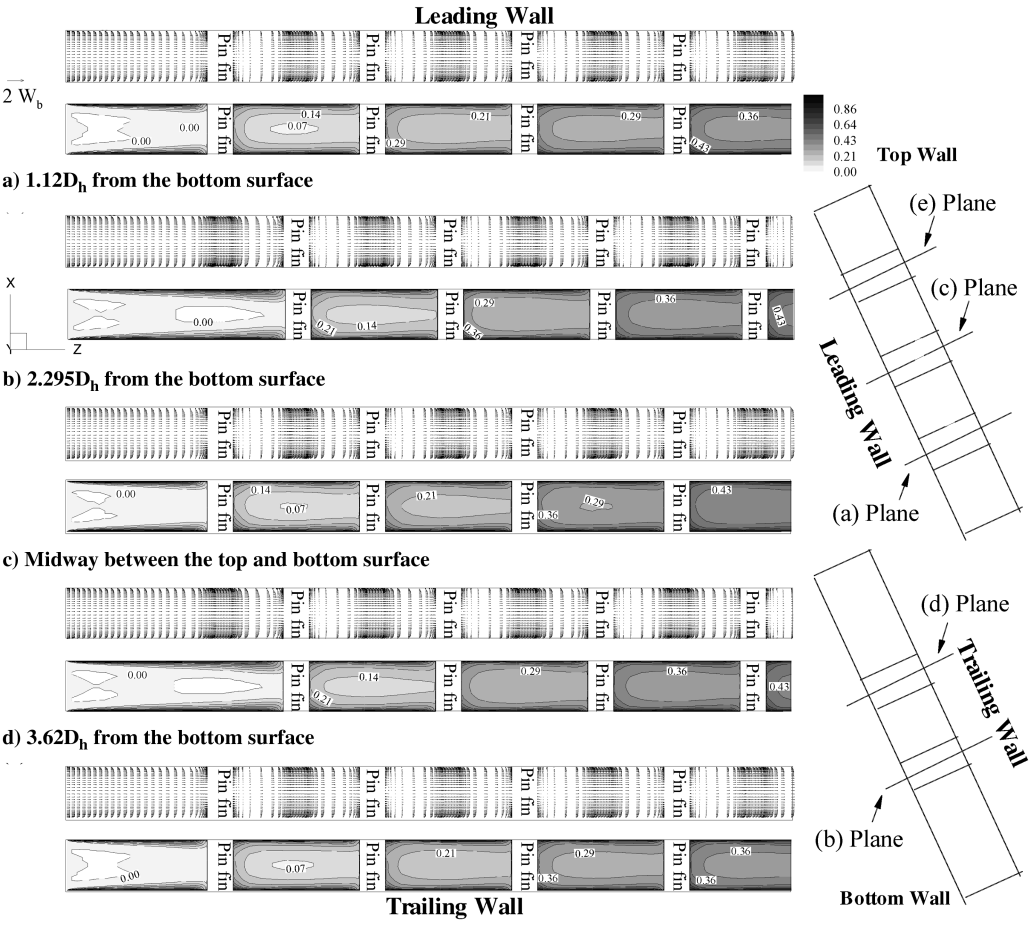

Fig. 8 Velocity vectors and dimensionless temperature $[\theta = (T - T_i)/(T_w - T_i)]$ contours. $Re = 10,000$, $Ro = 0.035$, $\beta = 120$ deg, and $\Delta\rho/\rho = 0.1$: a) $Y/D_h = 1.12$; b) $Y/D_h = 1.96$; c) $Y/D_h = 2.79$; d) $Y/D_h = 3.62$; e) $Y/D_h = 4.46$.

conjunction with the two-layer Reynolds stress turbulence closure model (RSM) are solved using the finite volume code FLUENT. The RSM turbulence model that we have chosen is primarily valid for turbulent core flows (i.e., the flow in the regions somewhat far from the walls). Therefore in this paper a two-layer model is used to calculate the flow variable in the near-wall region. The flow is considered to be incompressible since the Mach number is quite low. However, the density variations caused by the temperature difference and pressure gradient are approximated using ideal gas law. Physical properties of refrigerant R134a are used in the present simulation, to compare our results with Willett and Bergles [12]. All computations presented here were obtained by starting with the stationary case and then gradually increasing the rotation speed.

Results and Discussion

Pin fins are arranged in a staggered manner on heated walls of the channel, which is schematically presented in Fig. 1b. Because of this pin-fin arrangement, flow and heat transfer differs remarkably from that of the smooth channel due to the existence of the pin fins. Results for secondary flow vectors and dimensionless temperature are presented at axial locations $S/D_h = 3.36$ (first row), 5.00 (second row), 10.87 (midway between the fifth and sixth rows), 13.37 (at the eighth row), 12.54 (seventh row), and 15.00 (midway between sixth and seventh rows), respectively. The Reynolds number based on the channel hydraulic diameter is kept constant through the range of rotation numbers. Following Willett and Bergles [12], the Nusselt number is normalized using the Metzger correlation as follows:

$$Nu_o = 0.135\, Re^{0.64}(x/d)^{-0.34}$$

where d is the pin-fin diameter, and the Reynolds number Re is based on maximum velocity u_m, and x is the streamwise distance between the pin fins.

Velocity and Temperature Fields

Before discussing the detailed computed velocity field, a general conceptual view about the secondary flow patterns induced by pin fins and rotation is summarized and sketched in Fig. 3. The pin fins in the nonrotating duct (Fig. 3a) produce secondary flow that emanates upward and downward from each pin fin. For a plane across any three pin-fin row, the Coriolis force (Fig. 3b) produces four additional rotating vortices. Three of them are clockwise while the fourth one next to the bottom wall is counterclockwise. For a plane across any two pin-fin row (Fig. 3c), three rotating vortices appear; two of them are clockwise while the third one, next to the bottom wall, is counterclockwise. It is worth mentioning that this sketch is approximate because sometimes the rotation induced secondary flow significantly changes the pin-fin induced secondary flow, leaving the picture very mixed.

Figures 4–7 show the calculated secondary flow vectors and dimensionless temperature contours for the cases mentioned in Table 1 (at several axial locations as defined in Fig. 1b). For the stationary case, Fig. 4-I shows the calculated secondary flow vectors and dimensionless temperature contours at various axial locations. At the first axial location (Fig. 4a-I), secondary flow is from the pin-fin surfaces to either side. It is seen that the magnitudes of secondary flow vectors are high in the vicinity of the leading and the trailing walls and the low velocity vectors are observed in the top, bottom, and midregions between the pin fins; hence temperature gradient is high in the vicinity of the leading and the trailing walls that can be

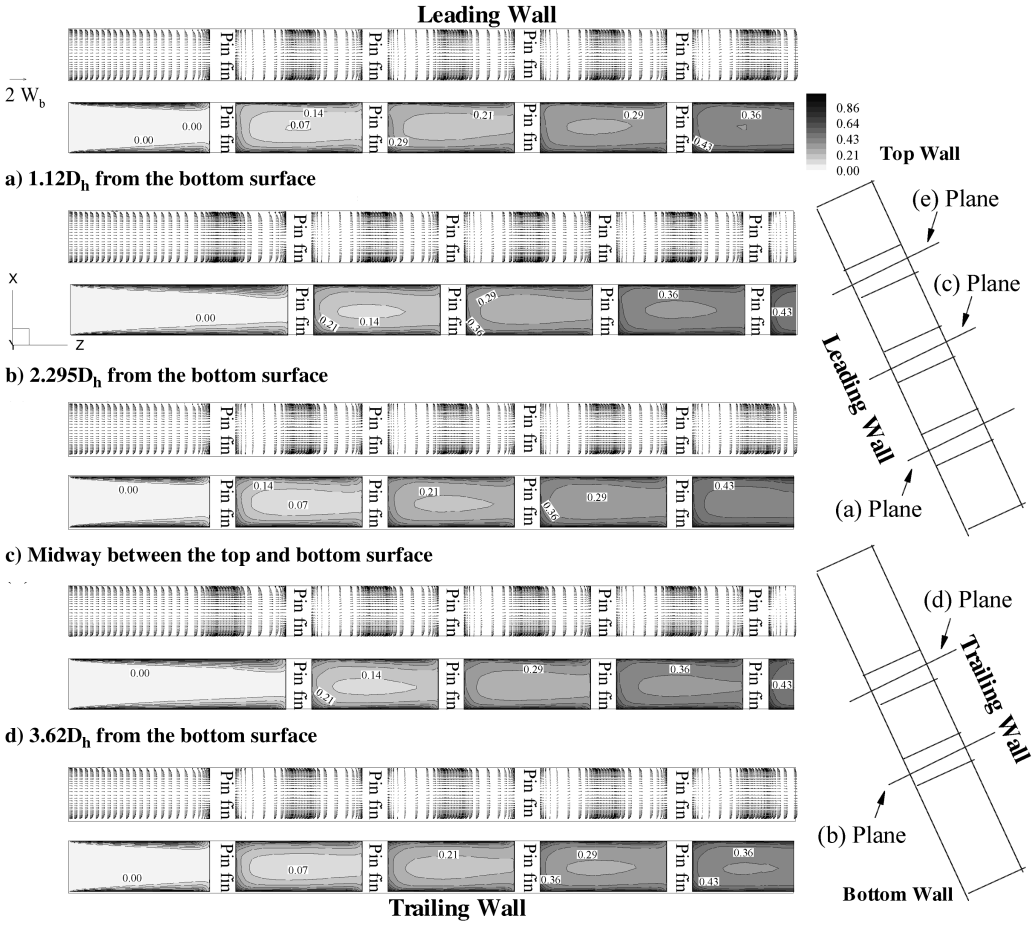

Fig. 9 Velocity vectors and dimensionless temperature $[\theta = (T - T_i)/(T_w - T_i)]$ contours. $Re = 10,000$, $Ro = 0.14$, $\beta = 120$ deg, and $\Delta\rho/\rho = 0.1$: a) $Y/D_h = 1.12$; b) $Y/D_h = 1.96$; c) $Y/D_h = 2.79$; d) $Y/D_h = 3.62$; e) $Y/D_h = 4.46$.

observed from corresponding dimensionless temperature field. Figures 4c and 4d-I show the secondary flow vectors and dimensionless temperature contours midway between the fifth and sixth, and sixth and seventh rows (wake regions) of the pin fins, respectively. Figure 4-II shows velocity vectors and dimensionless temperature contours. $Re = 10,000$ for $Ro = 0.035$, and $\Delta\rho/\rho = 0.1$ and $\beta = 90$ deg. From Figs. 4e–4h-II, the Coriolis force has almost no effect on the pin-fin induced secondary flow. Only downstream at the top and the bottom of the channel (Figs. 4g and 4h-II) does the Coriolis force have some appreciable effect on the pin-fin induced secondary flow. Therefore, it can be concluded that at this low rotation number the pin-fin induced secondary flow dominates over the Coriolis induced secondary flow. The temperature contours in this figure assert the negligible effect of rotation on the upstream temperature distribution while slight distortion to the temperature contours is seen downstream (Figs. 4g and 4h-II).

In Fig. 5, the angle orientation is changed to $\beta = 120$ deg, while keeping the rotation number and density ratio the same ($Ro = 0.035$, $\Delta\rho/\rho = 0.1$). It can be seen from Figs. 5c and 5d that the Coriolis force induced secondary flow has more room to develop (although slightly) compared to the pin-fin induced secondary flow. At planes midway between any two rows of pin fins, it can be seen from the same figure that the cooler fluid is pushed by Coriolis force action toward the bottom surface.

Figure 6 shows calculated secondary flow and dimensionless temperature contours for $Ro = 0.14$ keeping the remaining parameters the same as before. The Coriolis induced secondary flow is getting stronger and affecting the pin-fin induced secondary flow. This effect manifests more in the downstream sections as seen from the planes in Figs. 6c–6f.

Figure 7 shows calculated secondary flow and dimensionless temperature contours for density ratio $\Delta\rho/\rho = 0.4$, while keeping the rotation number fixed at $Ro = 0.14$ as well as the remaining parameters. As density ratio $\Delta\rho/\rho$ is increased to 0.4, the secondary flow and the temperature contour patterns increase in strength and magnitude, respectively. In planes across any three-pin-fin rows, a clockwise rotation induced vortex is generated above the top pin fin and in the interregions between pin fins (Figs. 7a and 7e). Below the bottom pin fin, a counterclockwise vortex can be seen resulting into strong distortion of the pin-fin induced secondary flow. For planes across two-pin-fin rows, a clockwise rotation induced vortex is generated above the top pin fin and in the interregion between the two pin fins (Figs. 7b and 7f). Below the bottom pin fin, the pin-fin induced secondary flow experiences a strong distortion due to a strong counterclockwise vortex.

Figures 8–10 show the streamwise velocity distribution and temperature contours at five planes parallel to the top/bottom surfaces. The planes are arranged on the basis of an increasing distance from the bottom surface. Planes a and b are $1.12D_h$ and $2.95D_h$ from the bottom surface, respectively, while plane c is midway between the top and bottom surfaces. Planes d and e are $1.2D_h$ and $2.95D_h$, from the top surface, respectively.

Figure 8 shows velocity vectors and dimensionless temperature contours for $Ro = 0.035$, $\beta = 120$ deg, and $\Delta\rho/\rho = 0.1$. The cold fluid in the core region is pushed slightly toward the trailing wall and the temperature field is seen to be slightly asymmetric. As the rotation number is increased to 0.14, keeping density ratio as before, the velocity gradient is found to be high on the trailing wall in the wake regions because the magnitude of flow velocity is low and hence Coriolis force pushes the fluid toward the trailing wall. In the other regions of the channel the effect of the Coriolis force appears to have no effect on the streamwise flowfield, which is evident from the calculated velocity vectors and the temperature field in Fig. 8. Further increase in rotation number and density ratio (Figs. 9 and 10) reveals

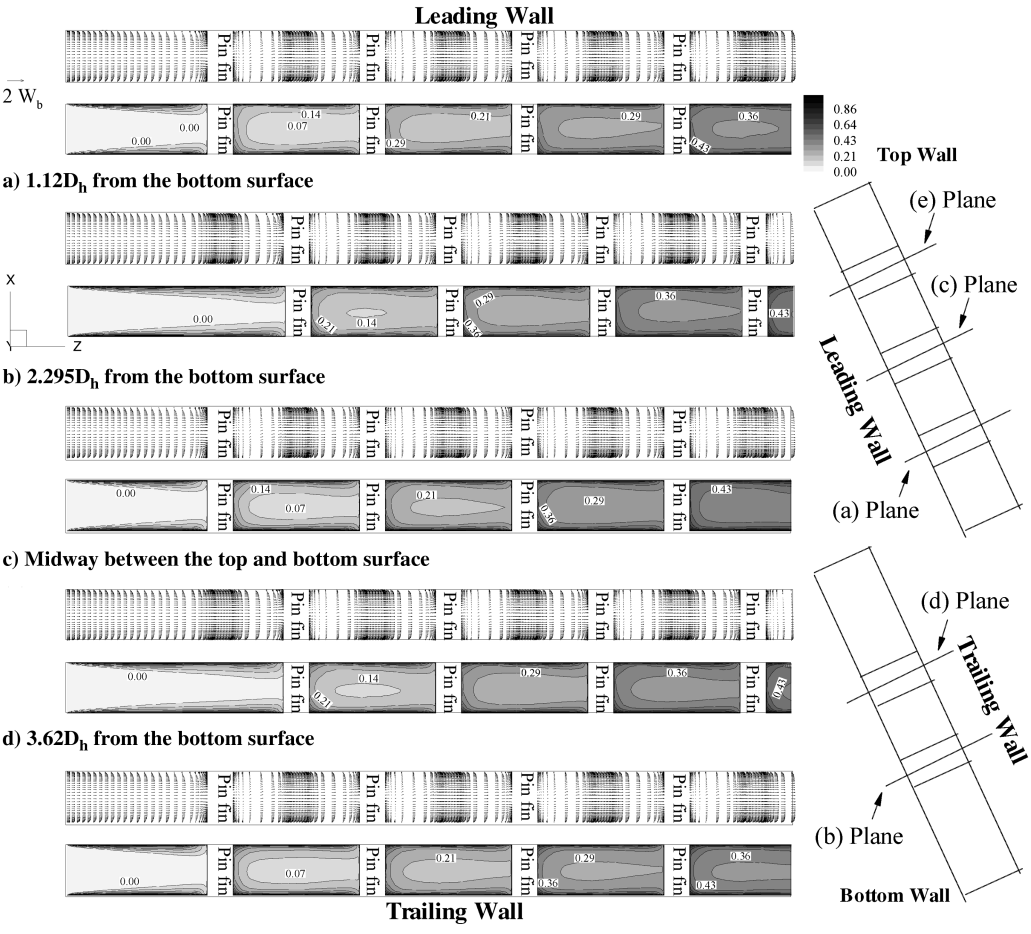

Fig. 10 Velocity vectors and dimensionless temperature $[\theta = (T - T_i)/(T_w - T_i)]$ contours. $Re = 10,000$, $Ro = 0.14$, $\beta = 120$ deg, and $\Delta\rho/\rho = 0.4$: a) $Y/D_h = 1.12$; b) $Y/D_h = 1.96$; c) $Y/D_h = 2.79$; d) $Y/D_h = 3.62$; e) $Y/D_h = 4.46$.

that almost no change occurs in the streamwise velocity and temperature fields. This can be attributed to the high aspect ratio, which leaves the fluid with much less room to move from the leading to the trailing side.

Detailed Local Heat Transfer Coefficient

Heat transfer results are presented here to depict the influence of Coriolis, buoyancy forces on the heat transfer characteristic in rotating channels. For various rotation numbers and density ratios, Figs. 11 and 12 show the local Nusselt number ratio contours of the leading and the trailing surfaces, respectively. Figure 11b (12b for the trailing surface) is for $\beta = 90$ deg while Figs. 11c–11g (12c–12g for the trailing surface) are for $\beta = 120$ deg.

Effect of Increasing the Rotation Number and the Density Ratio on the Leading Surface

Figure 11a shows the calculated Nusselt number ratios on the leading wall for the stationary case, $Ro = 0.0$. The following features can be noticed. At the inlet, the Nusselt number ratios are high and decrease gradually toward the first pin-fin row. This is because the boundary layers are thin at the entrance region and start to develop downstream. Nusselt number ratios are symmetric with respect to a plane midway between the top and the bottom surface. High Nusselt number regions are found at the stagnation points of each pin fin with the regions at the first rows being large and diminishing in size downstream. Low Nusselt number regions are found at the wake regions behind each pin fin with the regions at the last rows being large and merging together. Because the top and bottom walls are unheated, high Nusselt number ratios are found next to the top and bottom walls all the way to the end of the channel.

Figure 11b shows the calculated Nusselt number ratios on the leading wall for $\beta = 90$ deg, $Ro = 0.035$, and density ratio $\Delta\rho/\rho = 0.1$. It is seen that the Nusselt number contours are symmetric with respect to a plane midway between the top and bottom surfaces. This is expected because the channel orientation is orthogonal with respect to the direction of rotation. Compared to the stationary case, the contours of the Nusselt number ratios have lower values next to the top and bottom walls until the fourth row. When channel orientation is changed to $\beta = 120$ deg while keeping the rotation number and density ratios the same at 0.035 and 0.1 (Fig. 11c), respectively, it can be seen that the Nusselt number ratios lose symmetry with respect to the plane midway between the top and bottom walls. This can be seen by noticing that the low Nusselt

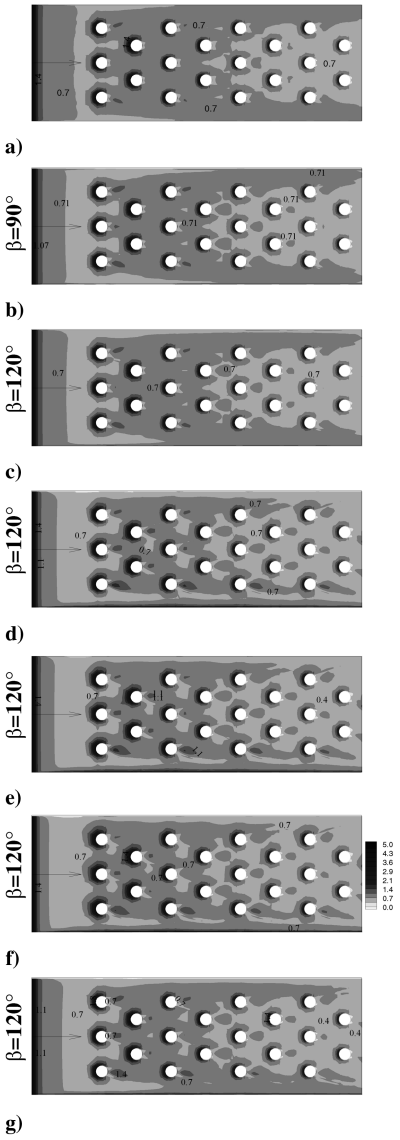

Fig. 11 Detailed Nusselt number distributions on leading walls. $Re = 10,000$. a) $Ro = 0.0$ and $\Delta\rho/\rho = 0.1$; b) $Ro = 0.035$ and $\Delta\rho/\rho = 0.1$; c) $Ro = 0.035$ and $\Delta\rho/\rho = 0.1$; d) $Ro = 0.07$ and $\Delta\rho/\rho = 0.1$; e) $Ro = 0.14$ and $\Delta\rho/\rho = 0.1$; f) $Ro = 0.14$ and $\Delta\rho/\rho = 0.2$; g) $Ro = 0.14$ and $\Delta\rho/\rho = 0.4$.

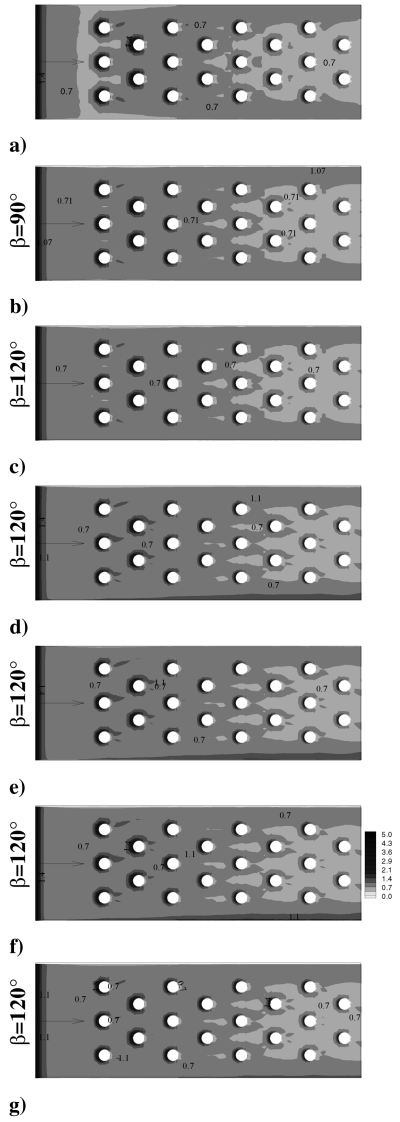

Fig. 12 Detailed Nusselt number distribution on trailing walls. $Re = 10,000$: a) $Ro = 0.035$ and $\Delta\rho/\rho = 0.1$; b) $Ro = 0.035$ and $\Delta\rho/\rho = 0.1$; c) $Ro = 0.07$ and $\Delta\rho/\rho = 0.1$; d) $Ro = 0.14$ and $\Delta\rho/\rho = 0.1$; e) $Ro = 0.14$ and $\Delta\rho/\rho = 0.2$; f) $Ro = 0.14$ and $\Delta\rho/\rho = 0.4$.

number ratios next to the top wall extend all the way to the channel exit while the low Nusselt number ratio regions next to the bottom wall extend only to the third row compared to the $\beta = 90$ deg case mentioned previously. Increasing the rotation number to 0.07 (Fig. 11d), it can be seen that the low Nusselt number ratios next to the top wall penetrate more in the spanwise direction. Also, one can observe the formation of small regions with high Nusselt number ratios approximately half a hydraulic diameter downstream of each pin fin. These regions increase in size and magnitude as we increase the rotation number further to 0.14 (Fig. 11e). Moreover, high Nusselt number ratios are seen to exist next to the bottom surface from inlet to exit. Now, we keep the rotation number fixed and increase the density ratios to 0.2 and 0.4, respectively, as shown in Figs. 11f and 11g. From those figures, the effect of the Coriolis force inducing secondary flow is seen to push cold fluid toward the bottom wall thus creating relatively high Nusselt number ratios.

Effect of Increasing the Rotation Number and the Density Ratio on the Trailing Surface

Comparing Fig. 12b ($Ro = 0.035$ and $\beta = 90$ deg) to the nonrotating case (Fig. 12a), it can be seen that the low Nusselt number ratios in front of the first row in the stationary case disappear in the rotating case. High Nusselt number regions are also found right before each pin fin with the regions at the first rows being large and diminishing in size downstream. Figures 12c–12g show the Nusselt number ratios for channel orientation of $\beta = 120$ deg. It is clear from these figures that high Nusselt number ratios onset near the bottom wall and grow from the downstream to the upstream as the rotation number and density ratios are increased. Moreover, high Nusselt number ratio regions are seen to increase areawise in front of each pin fin.

Spanwise Averaged Nusselt Number

Figure 13 shows the spanwise-averaged Nusselt number ratios both on leading and trailing walls for various cases of rotation numbers. The spanwise-averaged Nusselt number distributions on

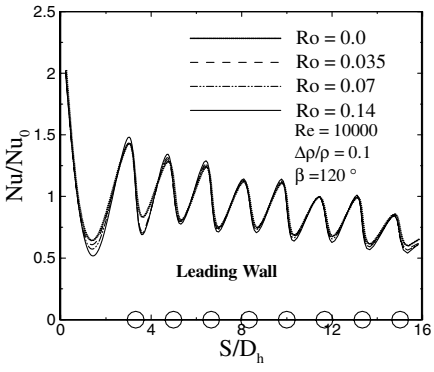

a)

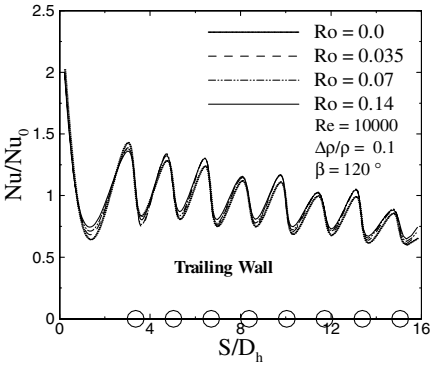

b)

Fig. 13 Spanwise-averaged Nusselt number. $Re = 10,000$, $\beta =$ 120 deg, and $\Delta\rho/\rho = 0.1$: a) leading wall; b) trailing wall.

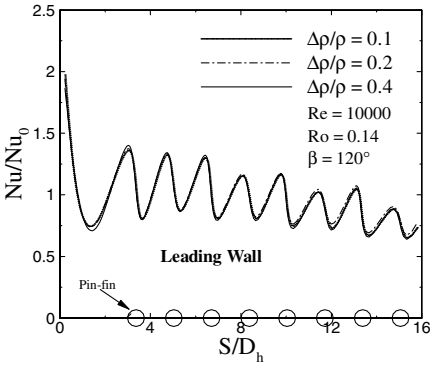

a)

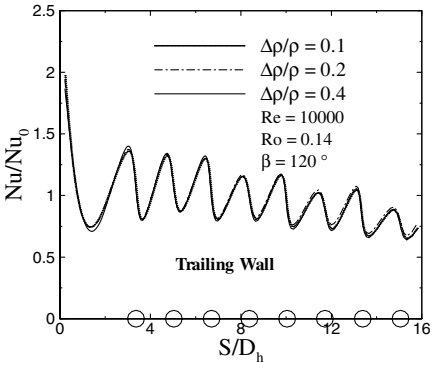

b)

Fig. 14 Spanwise-averaged Nusselt number. $Re = 10,000$, $\beta =$ 120 deg, and $Ro = 0.14$: a) leading wall; b) trailing wall.

the leading and trailing surfaces show periodic crests and troughs. The higher crests which occur just before the pin fins are caused by the flow impingement on the pin fins, and the lower troughs (which occur right after the pin fins) are caused by the flow reattachment after the pin fin. Between any two rows of pin fins, the Nusselt number ratios increase from the lowest value after any row of pin fins to the highest value right just before the next row of pin fins. The overall magnitude of the Nusselt number ratios decreases as it reaches the last row of pin fins. Right before the pin fins, the Nusselt number ratios on the leading wall increase with rotation (although slightly for the range of rotation numbers examined, $Ro = 0.035$–0.14). They decease with rotation right after the pin fin. The opposite is noticed on the trailing surface. Figure 14 shows the spanwise-averaged Nusselt number ratios both on the leading and trailing walls for various cases of density ratios. Similar periodic crests and troughs in the Nusselt number ratios can be seen in this figure. It can be stated that the density ratio does not have significant effect on the Nusselt number ratios.

Comparison with Experiment

To validate the results, we carried out extra simulation for rotation number Ro and density ratio $\Delta\rho/\rho$ similar to that of the experiments of Willet and Bergles [12], and results are shown in Tables 2 and 3. It can be seen that the computed Nusselt number is close to the

Table 2 Comparison of trailing Nusselt number ratios with experimental data [12]

Reynolds no., Re	Rotation no., Ro	Density ratio, $\Delta\rho/\rho$	Nu/Nu_o experiment	Nu/Nu_o present study
17,237	0.035	0.082	1.18	1.23
13,445	0.044	0.081	1.26	1.26
8,891	0.065	0.084	1.35	1.28
10,907	0.054	0.081	1.38	1.30
6,940	0.082	0.081	1.46	1.33

Table 3 Comparison of leading Nusselt number ratios with experimental data [12]

Reynolds no., Re	Rotation no., Ro	Density ratio, $\Delta\rho/\rho$	Nu/Nu_o experiment	Nu/Nu_o present study
11,038	0.053	0.078	1.16	1.22
8,994	0.065	0.081	1.25	1.24
7,169	0.081	0.083	1.36	1.26

experiment data of [12] and lies within a $\pm 15\%$ error band, for both the leading wall and the trailing wall. This difference can be attributed to the following. 1) The experiment boundary condition was a constant wall–heat–flux boundary condition while the present study uses constant surface temperature. 2) The uncertainty in experimental data is $\pm 11\%$.

Conclusions

The FLUENT code is used to predict flow and heat transfer in the rotating pin-finned channel with a high aspect ration (AR = 10) for various rotation numbers and inlet coolant-to-wall density ratios. Two channel orientations $\beta = 90$ and 120 deg are studied. A Reynolds stress model is used in conjunction with a two-layer model to compute flow variables. Flow and heat transfer in a pin-finned channel is complex geometry-wise and phenomena-wise. A secondary flow induced by pin fins is stronger when compared to Coriolis for low rotation number Ro. The average Nusselt number increases on the leading wall and decreases on the trailing wall with an increase in rotation number Ro. The average Nusselt number increases on both walls with an increase in density ratio $\Delta\rho/\rho$, up to a certain ratio, and then decreases.

Acknowledgments

This work was supported by the King Fahd University of Petroleum and Minerals (KFUPM) Funded Research Grant No. SAB 2003/04. This support is very much appreciated. The enlightening discussion at the beginning of this work by Laui Al-Hadhrami is also greatly appreciated.

References

[1] Metzger, D. E., Berry, R. A., and Bronson, J. P., "Developing Heat Transfer in Rectangular Ducts with Staggered Arrays of Short Pin-Fins," *Journal of Heat Transfer*, Vol. 104, No. 4, 1982, pp. 700–706.

[2] Metzger, D. E., and Haley, S. W., "Heat Transfer Experiments and Flow Visualization for Arrays of Short Pin-Fins," ASME Paper 82-GT-138, 1982.

[3] Metzger, D. E., Shepard, W. B., and Haley, S. W., "Row Resolved Heat Transfer Variations in Pin-Fin Arrays Including Effects of Non-Uniform Arrays and Flow Convergence," ASME Paper 86-GT-132, 1986.

[4] VanFossen, G. J., "Heat-Transfer Coefficients for Staggered Arrays of Short Pin-Fins," *Journal of Engineering for Power*, Vol. 104, No. 2, 1982, pp. 268–274.

[5] Brigham, B. A., and VanFossen, G. J., "Length to Diameter Ratio and Row Number Effects in Short Pin-Fin Heat Transfer," *Journal of Engineering for Gas Turbines and Power*, Vol. 106, No. 1, 1984, pp. 241–245.

[6] Chyu, M. K., and Goldstein, R. J., "Influence of an Array of Wall-Mounted Cylinders on the Mass Transfer from a Flat Surface," *International Journal of Heat and Mass Transfer*, Vol. 34, No. 9, 1991, pp. 2175–2186.

[7] Chyu, M. K., Hsing, Y. C., and Natarajan, V., "Convective Heat Transfer of Cubic Fin Arrays in a Narrow Channel," *Journal of Turbomachinery*, Vol. 120, No. 2, 1998, pp. 362–367.

[8] Chyu, M. K., Hsing, Y. C., and Shih, T. I.-P., "Heat Transfer Contributions of Pins and Endwall in Pin-Pin Arrays: Effects of Thermal Boundary Condition Modeling," ASME Paper 98-GT-175, 1998.

[9] Uzol, O., and Camci, C., "Elliptical Pin-Fins as an Alternative to Circular Pin-Fins for Gas Turbine Blade Cooling Applications, Part 1: Endwall Heat Transfer and Total Pressure Loss Characteristics," ASME Paper 2001-GT-0180, 2001.

[10] Hwang, J., and Lui, C., "Measurement of Endwall Heat Transfer and Pressure Drop in a Pin-Fin Wedge Duct," *International Journal of Heat and Mass Transfer*, Vol. 45, No. 4, 2002, pp. 877–888.

[11] Hwang, J., Lia, D. Y., and Tsia, J. P., "Heat Transfer and Pressure Drop in Pin-Fin Trapezoidal Ducts," ASME Paper 98-GT-110, 1998.

[12] Willett, F. T., and Bergles, A. E., "Heat Transfer in Rotating Narrow Rectangular Pin-Fin Ducts," *Experimental Thermal and Fluid Science*, Vol. 25, No. 7, 2002, pp. 573–582.

[13] Willett, F. T., and Bergles, A. E., "Heat Transfer in Rotating Narrow Rectangular Ducts with Heated Sides Oriented at 60° to the R-Z Plane," ASME Paper 2000-GT-224, 2000.

[14] Wright, L. M., Lee, E., and Han, J. C., "Effect of Rotation on Heat Transfer in Narrow Rectangular Cooling Channels (AR = 8:1 and 4:1) with Pin-Fins," ASME Paper GT2003-38340, 2003.

[15] Donahoo, E. E., Kulkarni, A. K., Belegundu, A. D., and Camci, C., "Determination of Optimal Row Spacing for a Staggered Cross-Pin Array in a Turbine Blade Cooling Passage," *Journal of Enhanced Heat Transfer*, Vol. 8, No. 1, 2001, pp. 41–53.

[16] Donahoo, E. E., Camci, C., Kulkarni, A. K., and Belegundu, A. D., "A Computational Visualization of Three Dimensional Flow: Finding Optimum Heat Transfer and Pressure Drop Characteristics from Short Cross-Pin Arrays and Comparison with Two-Dimensional Calculations," ASME Paper 99-GT-257, 1999.

[17] Hamilton, L. J., Adametz, D. S., Lind, E. K., and Gropinath, A., "Numerical Analysis of the Performance of a Staggered Cross-Pin Array Heat Exchanger," *Proceedings of the 8th AIAA/ASME Joint Thermophysics and Heat Transfer Conference*, AIAA, Reston, VA, 2002.

[18] Benhamadouche, S., and Laurence, D., "LES, Coarse LES, and Transient RANS Comparisons on the Flow Across a Tube Bundle," *International Journal of Heat and Fluid Flow*, Vol. 24, No. 4, 2003, pp. 470–479.

[19] Hassan, Y. A., and Barsamian, H. R., "Tube Bundle Flows with the Large Eddy Simulation Technique in Curvilinear Coordinates," *International Journal of Heat and Mass Transfer*, Vol. 47, No. 14, 2004, pp. 3057–3071.

[20] Su, G., Chen, H. C., and Han, J. C., "Computation of Flow and Heat Transfer in Rotating Rectangular Channels (AR = 4:1) with Pin-Fins by a Reynolds Stress Turbulence Model," ASME Paper GT2003-68390, 2005.

[21] Fluent-6 Manual. Fluent Inc., 2003.